

Model atmospheres and thermal spectra of magnetized neutron stars

Don A. Lloyd

Harvard-Smithsonian Center for Astrophysics, 60 Garden Street, Cambridge, MA 02138
email: dlloyd@cfa.harvard.edu

16 November 2018

ABSTRACT

Thermal surface radiation has been detected with X-ray instruments for several neutron stars with high spectral, spatial and timing resolution. These observations allow for direct study of fundamental properties of the source, but require model atmospheres and spectra for careful interpretation. We describe a robust and extensible implementation of complete linearization for computing the spectra of isolated cooling neutron stars for a broad range of temperature and magnetic field. Self-consistent spectra are derived for arbitrary magnetic field geometries at $B \leq 10^{14}$ G.

Key words: stars: neutron – stars: atmospheres – radiative transfer – methods: numerical – polarization – magnetic fields

1 INTRODUCTION

Isolated neutron stars (NSs) are most commonly discovered as radio pulsars and only infrequently as soft X-ray sources or through associations with supernovae. Cooling of the hot, isothermal NS core ($T_c \sim 10^9$ K) proceeds initially by neutrino diffusion, followed by an extended period of thermal emission at soft X-ray energies. In this latter phase, conduction in the insulating iron crust gives way to photon diffusion and free propagation of radiation through the tenuous outer layers of the NS atmosphere. The thermal evolution of NS has been the subject of much theoretical consideration since the seminal work of Tsuruta (1964), and Chiu & Salpeter (1964). In principal, measurement and interpretation of thermal X-rays emitted at the NS surface provides direct evidence of the star's surface composition, magnetic field properties, and, in the absence of reheating, may constrain the cooling history of the NS population or the equation of state of the stellar core. In practice, detection of these thermal X-rays is difficult. The stellar environment is energetic, particularly for young NS, and non-thermal emission processes which originate in the active pulsar magnetosphere dominate the surface radiation. Young pulsars may be obscured by diffuse non-thermal X-ray emission from the supernova remnant or from bright compact nebulae (plerions) driven by pulsar winds. Some NS are exceptionally luminous in thermal X-rays possibly owing to either a highly transparent surface composition or to reheating processes which maintain their core temperature, while the thermal and (brighter) non-thermal emissions for some cooling NS decline presumably at different rates until the surface radiation can be distinguished at late times.

The fundamental properties of NS thermal radiation are regulated by the source luminosity, the strong surface gravity of the star, and the composition of the atmosphere which is likely determined by either accretion (from the interstellar

medium, a fossil debris disk or stellar companion) or fall-back of supernova ejecta. Provided accretion is neither too great nor continuous, gravitational settling of heavy elements occurs on short timescales (Brown, Bildsten & Rutledge 1998), leaving the lightest elements to form the X-ray photosphere; only a tiny fraction of the stellar mass in these light elements is necessary to form an optically thick layer. Spectral reprocessing by the light element plasma atmosphere produces surface emission which differs substantially from the blackbody function regardless of magnetic field (Romani 1987; Rajagopal & Romani 1996; Zavlin, Pavlov & Shibano 1996b; Lloyd, Hernquist & Heyl 2003), and these discrepancies motivate the accurate computation of model atmospheres and spectra. Tabulations of unmagnetized NS X-ray spectra are now available in the XSPEC software (Pavlov et al. 1992; Zavlin et al. 1996b; Gänsicke et al. 2002), allowing for immediate comparison with the blackbody model for $B \lesssim 10^{10}$ G. The optical and near UV thermal flux shows strong dependence on both composition (Pavlov et al. 1996) and magnetic field strength (Lloyd et al. 2003). The most persuasive models for NS thermal radiation must reconcile the X-ray spectrum with optical and UV fluxes whenever possible.

Several codes have been developed to calculate the atmospheric structure and associated thermal spectrum for a variety of NS surface compositions and magnetic field regimes. The atmosphere is described by the self-consistent solution to a system of radiative transfer equations and equilibrium constraints. Essentially all methods for calculating radiative transport in magnetized NS atmospheres proceed from the work of Gnedin & Pavlov (1975), who established the connection between the density-matrix formalism and the (more immediately tractable) formulation of radiative transport in two coupled “normal” polarization modes; i.e., the limit of large Faraday depolarization. The plasma is strongly polarizing to

X-ray radiation at magnetic field strengths comparable to those of radio pulsars. The optical and UV spectra of such NS are also polarized for modest B , but measurement at these wavelengths is difficult owing to the presence of non-thermal radiation, absorption in the interstellar medium, and the overall faintness of the sources. The large plasma anisotropies induced by magnetic fields strongly affect the angular distribution of the emergent radiation field of the atmosphere, and a complete model of the thermal X-ray emission of a typical NS requires integration over intensity profiles from surface elements having local temperature and magnetic field which vary across the stellar surface (Zavlin et al. 1995a). All modern strategies appeal to the full angle and energy dependence of the plasma opacity and coupled radiation field.

Early efforts to model the X-ray emission from NS atmospheric plasma were preceded by the development of the radiative transfer by the normal mode approximation in uniform (isothermal) plasma slabs (Kaminker et al. 1983) using the normal mode strategy of Gnedin & Pavlov (1975) to describe the radiative diffusion. Shibano et al. (1992) applied the diffusion method of Kaminker et al. (1983) to NS atmospheres with fully ionized H/He mixtures by implementing the constraints of hydrostatic and radiative equilibrium. Pavlov et al. (1994) computed spectra for generally oblique magnetic fields the NS atmosphere from the thermal structures from Shibano et al. (1992) by recalculating the plasma opacities and making a formal integration of the transfer equation from the prior solution. Pavlov et al. (1995) improved the diffusion results by using them as an approximate solution to the temperature correction procedure of Auer & Mihalas (1968); this work also included a prescription for the ionization equilibrium of the Hydrogen plasma (see also Zavlin & Pavlov (2002)).

Romani (1987) described the first self-consistent NS model atmospheres for weak magnetic fields using the Los Alamos Opacity Library and some simplifying assumptions about the relative contribution of thermal and scattering emissivities. In this method, the radiation field is derived from application of the Milne integral operator to the source function and temperature corrections to the atmospheric structure were evaluated by the Lucy-Unsöld method (Mihalas 1978). Rajagopal & Romani (1996) revisited this work using the OPAL tabulations (Iglesias et al. 1992) while Rajagopal et al. (1997), using essentially the same formalism, extended their opacity model to roughly approximate the bound state transitions in magnetized iron, and included electron scattering and free-free absorption in the normal mode approximation. Each of these efforts revealed the extent of compositional effects on the thermal X-ray spectra of He, Fe and cosmic abundance atmospheres. More recently, Gänsicke et al. (2002) have revisited the low-field regime using these methods to consider reheating in the outer atmospheric layers of some NS. Werner & Deetjen (2000) have taken a different computational approach, deriving the first non-LTE model calculations in the weak field regime using the Accelerated Lambda Iteration combined with the Opacity Project cross sections; these authors find modest corrections due to NLTE effects in light element plasma at low temperatures, but these are potentially more significant for magnetic fields stronger than they consider. Some recent modeling efforts have specialized to the calculation of light element “magnetar” spectra ($B \gtrsim 10^{14}$ G) which include some prescription for vacuum polarization effects which are particularly relevant for $B \gtrsim 4.4 \times 10^{13}$ G. Zane et al. (2000) considered in particular atmospheres heated externally at low accretion rates, generalizing energy balance in the atmosphere to account for energy deposition by charged particles. Özel (2001) and Ho & Lai (2001) have each generalized the the Lucy-Unsöld

method to the normal mode approximation to derive model spectra for highly magnetized, light element NS plasma. Ho & Lai (2001) also considered the diffusion equation solutions to perpendicular (normal) and parallel magnetic field geometries in the intense field regime.

This article describes an implementation of the classical technique of complete linearization (CL) to the modeling of elementary NS atmospheres in radiative equilibrium. We restrict our derivation to model atmospheres with pure Hydrogen composition in the limit of complete ionization, but the formulation is immediately useful to admixtures of Helium. The method is robust, flexible with respect to the range of model parameters for which it can be applied, and is extensible to detailed statistical equilibrium for partially ionized models and complete Stokes transport. Self-consistent model results for magnetic fields $B \leq 10^{14}$ G and of arbitrary field orientation, and a range of flux temperatures characteristic of NS observed in thermal X-rays have been calculated with this methodology. The article is organized as follows: The magnetized plasma opacity is derived in §2, with attention to the role of protons and vacuum effects in radiative processes. The radiative transfer equations and their constraints are derived in §3. The grid methods and solution techniques are described in §4. An abbreviated selection of model results are presented in §5, and emphasize the angular intensity properties and spectral characteristics, including polarization for the weak, intermediate and strong field regimes. Extensions and limitations of the present method are outlined in §6.

2 OPACITY AND EMISSIVITY OF MAGNETIZED PLASMA

The detailed polarizing properties of a light element magnetized plasma can be derived from its dielectric response to electromagnetic waves. This presentation is similar to that found in Ventura (1979) and Mészáros & Ventura (1979). The equation for an electromagnetic wave propagating in a medium of refractive index N along the direction \hat{k} , including the vacuum permeability, is

$$\left[-aN^2(\vec{1} - \hat{k}\hat{k}) + hN^2(\hat{k} \times \hat{b})(\hat{k} \times \hat{b}) + \epsilon \right] \vec{E} = 0 \quad (1)$$

where $\hat{b} = (\sin \theta, 0, \cos \theta)$ is the unit vector in the direction of \vec{B} , and a and h are defined below. For uniformly magnetized cold plasma, the vacuum corrected dielectric in the $\vec{B} \parallel \hat{z}$ frame is

$$\epsilon' = \begin{pmatrix} \epsilon & ig & 0 \\ -ig & \epsilon & 0 \\ 0 & 0 & \eta \end{pmatrix} \quad (2)$$

and has tensor elements

$$\epsilon = a - \sum_s \frac{\lambda_s v_s}{\lambda_s^2 - u_s} \quad (3)$$

$$g = - \sum_s \frac{v_s u_s^{1/2}}{\lambda_s^2 - u_s} \quad (4)$$

$$\eta = a + q - \sum_s v_s / \lambda_s \quad (5)$$

in which the plasma and cyclotron frequencies for each species enter through the parameters

$$v_s = (\omega_{p,s}/\omega)^2 \quad (6)$$

$$u_s^{1/2} = (\omega_{c,s}/\omega) \quad (7)$$

for $\omega_{p,s}^2 = 4\pi e^2 n_s / m_s$ and $\omega_{c,s} = q_s B / (m_s c)$; note that $u_s^{1/2}$ is a signed quantity. The damping term $\lambda_s = 1 + i\nu_s / \omega$ splits the plasma dielectric into hermitian and anti-hermitian contributions, but when evaluating the polarization of propagating waves it is acceptable to consider only the hermitian part of the dielectric. The parameters a, h and q are functions solely of the magnetic field strength:

$$a(x) = 1 + \frac{\alpha}{2\pi} [-2X_0(x) + xX'_0(x)] \quad (8)$$

$$h(x) = \frac{\alpha}{2\pi} [x^2 X''_0(x) - xX'_0(x)] \quad (9)$$

$$q(x) = -\frac{\alpha}{2\pi} X_1(x) \quad (10)$$

where $x \equiv B_Q / B$, $B_Q \equiv m_e^2 c^3 / (e\hbar) \simeq 4.4 \times 10^{13}$ G is the quantum critical field strength, and the functions X_0 and X_1 are found in Heyl & Hernquist (1997); the expressions (8-10) are valid for all field regimes and revert to the results of Mészáros & Ventura (1979) in the weak field limit, $x > 1$. The tensor ϵ in the $\hat{k} \parallel \hat{z}$ frame is recovered from (2) by an orthogonal transformation of angle $\cos \theta = \hat{k} \cdot \hat{b}$ about the $\hat{k} \times \hat{b}$ axis.

The polarization vector for an EM wave in mode j in rotating coordinates about the magnetic field is

$$\vec{e}^j = \left(\frac{1}{\sqrt{2}} [K_x^j \cos \theta - K_z^j \sin \theta \pm i], K_z^j \cos \theta + K_x^j \sin \theta \right) \quad (11)$$

where the component indices are $(\pm, 0)$, respectively. The normal modes are usually referred to as ordinary (O) and extraordinary (X); waves propagating in the ordinary mode are largely unaffected by the magnetic field, while X mode radiation with $\omega < \omega_{c,e}$ propagates with a reduced refractive index. Adopting the notation $j = (1, 2)$ to label mode (X,O) respectively, the transverse ellipticity may be expressed compactly:

$$K_x^j = \frac{i\zeta}{b + (-1)^{3-j} \text{sgn}(y) \sqrt{b^2 + \zeta}} \quad (12)$$

where

$$b = \frac{x \sin^2 \theta}{2g\eta \cos \theta} \quad (13)$$

$$x = \varepsilon^2 - g^2 - \varepsilon\eta(1 - h/a) \quad (14)$$

$$y = \frac{x \sin^2 \theta}{a(\varepsilon \sin^2 \theta + \eta \cos^2 \theta)} \quad (15)$$

$$\zeta = 1 - h \sin^2 \theta / a \quad (16)$$

and the longitudinal polarization component has ellipticity given by:

$$K_z^j = -\frac{[ig + (\varepsilon - \eta)K_x^j \cos \theta] \sin \theta}{\varepsilon \sin^2 \theta + \eta \cos^2 \theta} \quad (17)$$

2.1 Cross sections

The principal opacity sources in a fully ionized, light element plasma are the free-free absorption and ordinary Thomson scattering. The differential cross-section for scattering by electrons of photons with momentum k in polarization mode i into momentum k' and mode j is (Ventura 1979):

$$\left(\frac{d\sigma_{ij}^{kk'}}{d\Omega} \right) = \frac{k'}{k} r_0^2 |\hat{e}', \Pi^{(p)} \cdot \hat{e}|^2 \quad (18)$$

where $r_0 = e^2 / (mc^2)$ is the classical electron radius (cm). Super-script (p) denotes plasma components only; e.g. the plasma polarization tensor is

$$\Pi^{(p)} = v_e^{-1} (\delta - \epsilon^{(p)}) \quad (19)$$

The eigenvalues of (19) for the plasma component of the total dielectric (2) are

$$\pi_{\pm} = v_e^{-1} [1 - \epsilon^{(p)} \pm g^{(p)}]$$

$$\pi_0 = v_e^{-1} [1 - \eta^{(p)}]$$

To excellent approximation, the squared eigenvalues can be written compactly as a rational expression in terms of the plasma constituents; including the damping term $\gamma_s \equiv \nu_s / \omega$ these are:

$$\pi_p^2 = \frac{(\sum_s m_e / m_s)^2}{\prod_s \left[(1 - p u_s^{1/2})^2 + \gamma_s^2 \right]} \quad (20)$$

For coherent scattering, eqn (18) is a sum over polarization components p , and has a scale fixed by the Thomson cross section $\sigma_T = 8\pi r_0^2 / 3$:

$$\left(\frac{d\sigma_{ij}^{kk'}}{d\Omega} \right) = \sigma_T \left[\frac{3}{8\pi} \sum_{p=-1}^{+1} |e_p^j(k')|^2 |e_p^i(k)|^2 \pi_p^2 \right] \quad (21)$$

Integration of (21) over final momenta k' yields the partial cross-section to mode i photons which scatter into momentum k and mode j

$$\sigma_{ij}(k) = \sigma_T \left[\frac{3}{8\pi} \int_{\Omega'} d\Omega' \sum_{p=-1}^{+1} |e_p^j(k')|^2 |e_p^i(k)|^2 \pi_p^2 \right] \quad (22)$$

The bracketed term is the geometric correction to the scattering process induced by the magnetic field in the mode conserving ($i = j$) or mode crossing channels ($i \neq j$). The damping factor γ_s is obtained from the sum of the radiative and collisional damping frequencies:

$$\nu_{s,rad} = 2(e\omega)^2 / (3m_s c^3)$$

$$\nu_{s,coll} = \alpha_0 \nu_{rad} / (n_s \sigma_T)$$

where the free-free absorption coefficient α_0 is defined below. Damping is only relevant near the resonant frequencies of π_{\pm}^2 , i.e., $\omega \simeq \omega_{c,s}$.

The total electron scattering cross-section to mode i photons is obtained by summing (22) over final polarization j .

$$\begin{aligned} \sigma_i(k) &= \sigma_T \left[\frac{3}{8\pi} \int_{\Omega'} d\Omega' \sum_{j=1}^2 \sum_{p=-1}^{+1} |e_p^j(k')|^2 |e_p^i(k)|^2 \pi_p^2 \right] \\ &\equiv \sigma_T G_i(k) \end{aligned} \quad (23)$$

The magnetic free-free absorption coefficient is similarly derived; the total absorption for mode i photons is:

$$\begin{aligned} \alpha_i^{ff}(k) &= \alpha_0 \left[\frac{3}{8\pi} \int_{\Omega'} d\Omega' \sum_{j=1}^2 \sum_{p=-1}^{+1} g_p |e_p^j(k')|^2 |e_p^i(k)|^2 \pi_p^2 \right] \\ &\equiv \alpha_0 G_i^{ff}(k) \end{aligned} \quad (24)$$

where g is the Gaunt factor and α_0 is the absorption coefficient in the zero field limit, corrected for stimulated emission:

$$\alpha_0 = n_e n_i Z^2 \frac{4e^6}{3m_e h c} \left(\frac{2\pi}{3m_e k T} \right)^{1/2} \nu^{-3} (1 - e^{-h\nu/kT}) \quad (25)$$

The corresponding emissivity is related to the absorption coefficient through the Einstein rate coefficients; i.e., Kirchoff's law:

$$j_{\nu,ff}^i = n_e n_i Z^2 \frac{8e^6}{3m_e c^3} \left(\frac{2\pi}{3m_e kT} \right)^{1/2} e^{-h\nu/kT} G_i^{ff}(k) \quad (26)$$

Equation (26) is the correct thermal emissivity of unmagnetized plasma; for arbitrarily magnetized plasma, the expression must be multiplied by 0.5 to obtain the emissivity *per mode*. In the polarizing medium, thermal emissivity is greater for the more opaque mode. It is convenient to scale the opacity and emissivity by the local mass density:

$$\chi_\nu^i = \frac{\alpha_i^{ff} + n_e \sigma_i}{\rho} \text{ cm}^2 \text{ g}^{-1} \quad (27)$$

$$\eta_\nu^i = \frac{j_{\nu,th}^i + j_{\nu,sc}^i}{\rho} \text{ erg g}^{-1} \text{ s}^{-1} \text{ Hz}^{-1} \text{ sr}^{-1} \quad (28)$$

The thermal emissivity j_i^{th} is given by eqn (26), and the scattering emissivity in mode i is

$$j_{\nu,sc}^i(k) = n_e \int_{\Omega'} d\Omega' \sum_{j=1}^2 u^j(k') \left(\frac{d\sigma_{ji}^{k'k}}{d\Omega'} \right) \quad (29)$$

where the integration is performed over incoming photon momenta.

For unmagnetized plasma, the Gaunt factors and their derivatives are evaluated from the fitting formulae of Itoh et al. (2000) or the tabulations of Sutherland (1998). The magnetic Gaunt factors and their temperature derivatives are evaluated by the integral expressions found in Kirk & Mészáros (1980); this calculation proceeds from an average of the ground state Coulomb matrix elements over a one-dimensional electron distribution in the Landau ground level, which adequately describes the available electronic states in highly magnetized plasma. In weak magnetic fields, we expect that the anisotropy of the electron distribution is sufficiently mild in this regard to allow substitution of the Gaunt factors $g_{\pm,0}$ with the zero-field values. The transition from the classical to quantizing magnetic field regimes is characterized by the parameter

$$\ell = k T_{eff} / (\hbar \omega_{c,e}) \simeq 7.4 \times 10^3 T_{eff} / B \quad (30)$$

which is computed from the effective temperature T_{eff} defined in §3 and neglecting variation in local temperature in a realistic atmosphere. In this formulation the Gaunt factors are incompletely calculated over a range of (T_{eff}, B) corresponding to the transition between the classical field and strongly magnetized regimes $\ell \sim \mathcal{O}(1)$.

The geometric correction factors $G_i(k)$ and $G_i^{ff}(k)$ in (23) and (24) are fundamental quantities in the opacity calculations which fully describe all resonant behaviors of the magnetized plasma through self-consistent inclusion of ions and vacuum in the dielectric (2), and which are computed explicitly for all model photon energies and trajectories. The cross sections are invariant to reversal of the magnetic field direction, and each cyclotron line has an effective width $\Delta\omega_{c,s} \propto \omega_{c,s}$ in excess of either the thermal or natural width γ_s of the resonance. Note that our choice for $\Pi^{(p)}$ generalizes the polarization tensor for the multi-component plasma and produces the expected resonances at the electron and ion cyclotron frequencies. The vacuum dielectric influences only the calculation of the polarization vectors (11) with consequences discussed below. Cross sections for direct absorption and scattering by ions are reduced from their respective electronic values by a factor $\mathcal{O}(m_e/m_p)^2$ and may be neglected without consequence when calculating the opacity. The opacity to radiation in parallel propagation to the magnetic field is approximately identical in

each mode, regardless of the magnitude of the vacuum corrections to the plasma response; substantial differences in the differential cross sections can produce unequal intensities and finite polarization along magnetic field lines.

Electron and ion cyclotron absorption each result from different functional properties of the magneto-geometric factors. Both features are sensitive to projection of the X mode polarization vectors onto the circular basis about the magnetic field (11). In the electron feature, projection over all angles onto the resonant eigenvalue π_\perp^2 is complete; therefore only radiation in X mode is resonantly absorbed while the O mode has no projection on π_\perp^2 and is consequently insensitive to resonant absorption. At frequencies $\omega \ll \omega_{c,e}$ the \hat{e}_0^X is everywhere zero except near either ion cyclotron frequency where it resonantly acquires a finite projection. Owing to the large relative opacity to waves polarized parallel to the magnetic field at these frequencies, it is this “polarization vector” resonance which dominates the total opacity to X mode radiation in the ion cyclotron resonance. The polarization structure in the resonance is complicated further by the abrupt exchange of \pm components at a critical frequency near $\omega_{c,p}$ (Bulik & Pavlov 1996), but the magnitude of the circular components remains symmetric across the feature.

The magnetic field provides a preferred orientation to scattering and absorption processes, resulting in anisotropic plasma response and finite polarization of propagating radiation. The magnitude of these effects scale principally with $u_e = (\omega_{c,e}/\omega)^2$. Ion cyclotron features arise independent of vacuum corrections from a parametric resonance between electrons and ions in the dielectric tensor. Moreover, any additive contributions to the total plasma dielectric (e.g. line or ionization transitions) introduce additional polarization resonances. The electronic and ionic plasma constituents cannot be consistently treated as independent entities.

2.2 Vacuum resonance and mode ambiguity

In the previous section, formation of the ion cyclotron resonance was shown to arise primarily from a critical parametric phenomenon in the spectrum of the polarization vector components, \hat{e}_p^j . This is one example of the more generic competition between multiple sources of polarizability in magnetized plasma. More generally, any additive component to the dielectric (2) (e.g. transitions in neutral atoms) can produce other resonant behaviors, and introduce additional complexity to the spectrum of critical behavior. In intense magnetic fields ($B \gtrsim B_Q$), vacuum polarizability has a significant influence on the X-ray plasma opacities, and possesses parametric polarization resonances analogous to those of ion cyclotron lines. Birefringence of the magnetized vacuum has been investigated by many authors (e.g. Adler (1971) for review and Pavlov & Shibano (1979) for discussion relevant to NS applications); strictly, the effect remains finite for arbitrarily weak fields although, to excellent approximation, the vacuum corrections to weakly magnetized plasma are identical to the uncorrected (pure) plasma. Our discussion of the vacuum effect proceeds from the work of Soffel et al. (1983).

Inspection of (12) reveals that the transverse ellipticities of the two modes are identical for arbitrary θ when $b = \pm i\sqrt{\zeta} \rightarrow K_x^j = \pm b$. This is distinct from (e.g.) the case of parallel propagation ($\hat{k} \parallel \vec{B}$) in which the modes are circular, having identical *magnitude*, but opposite and unambiguous handedness. Where this occurs in a radiative transfer calculation, it may be impossible to uniquely specify the polarization content of the affected radiation field in two normal modes, sometimes called “mode collapse”. To

understand the limitation of our model calculations, it is necessary to investigate the plasma conditions under which the mode definition (12) is rendered ambiguous. To deduce the critical density at which mode collapse occurs, it is sufficient to study the necessary condition that $\text{Re}(b) = 0$ for arbitrary propagation angles, i.e. where $x = 0$ (eqns (13-14)). To first order in the fine-structure constant, this condition is satisfied to good approximation when

$$v_{res} = (q - h) \left(\frac{u_e - 1}{u_e} \right) \quad (31)$$

The critical density (31) is undefined for $\omega > \omega_{c,e}$ and photon frequencies in this range are insensitive to vacuum resonance effects at all plasma densities. For photons $\omega < \omega_{c,e}$, the resonant density (31) delineates a transition from the plasma dominated dielectric response into the vacuum dominated regime. For polarization vector calculations which invoke only real valued b , the modes acquire a finite but insubstantial measure of non-orthogonality when $b = 0$:

$$\left| \hat{e}_t^{1*} \cdot \hat{e}_t^2 \right| = h \sin^2 \theta / a \ll 1$$

where the transverse components $\hat{e}_t^j \equiv (\vec{1} - \hat{k}\hat{k}) \cdot \hat{e}^j$. When computing radiative transfer in such a medium, the mode identities remain distinct. Equation (31) is a quadratic expression for two critical frequencies which are responsive to the vacuum resonance at a given plasma density:

$$\omega_{\pm}^2 = \frac{\omega_{c,e}^2}{2} \left[1 \pm \sqrt{1 - \frac{4}{q-h} \left(\frac{\omega_{p,e}}{\omega_{c,e}} \right)^2} \right] \quad (32)$$

($q > h$) for all B and the critical frequencies are defined only for $\omega_{p,e}^2 < \omega_{c,e}^2(q-h)/4$. For $v > v_{res}$ the opacity is essentially unchanged from the pure plasma calculation and this regime is said to be *plasma dominated*. In the *vacuum dominated* regime ($v < v_{res}$) the modes become strictly linear, albeit slightly non-orthogonal, for all propagation angles $\theta > 0$, while both modes are fully circular for $\theta = 0$ in all circumstances. An additional consequence of conversion to linear polarization is that the angular dependence to the opacity in each mode is quenched in the vacuum regime. This implies that radiation decoupled from the plasma in the regime $v_{res} \gtrsim v(\tau_v = 1)$ will also become isotropized but, as we find in §5.3, this possibility is not realized in model atmosphere solutions.

The imaginary part of b is approximately

$$\text{Im}(b) \simeq \gamma_e \sqrt{u} \left[1 - \frac{2}{u-1} \right] \frac{\sin^2 \theta}{2 \cos \theta} \quad (33)$$

For magnetic field strengths capable of inducing the resonant phenomenon in NS atmospheres, the critical frequency $\omega_+ \simeq \omega_{c,e}$ is well above the limit of measurable thermal emission. Evaluating (33) at the low frequency resonance and taking $\text{Im}(b) = \sqrt{\epsilon}$, we find the critical angle at which the modes collapse at ω_- is $\cos \theta_- \simeq 0.5 \text{Im}(b) \ll 1$, or $\theta_- \simeq \pi/2$. $\text{Im}(b)$ is a rapidly varying function near the critical angle, and for only a very narrow range of $\theta \simeq \theta_-$ will the polarization modes become indistinguishable.

In the vacuum regime, the two critical frequencies are $\omega_+ \simeq \omega_{c,e}$ and $\omega_- < \omega_+$. Both polarization modes become sensitive to the electron cyclotron resonance in the vacuum dominated regime; this is however of no special consequence for our NS spectra where $\omega_{c,e}$ is unobservable for magnetic fields capable of producing the resonance behavior. From eqns (31) and (32) we find that, for a particular magnetic field strength B , there are two critical frequencies,

while, for any particular photon energy, the vacuum resonance core is found at a specific plasma density n_e .

Presently, no NS model atmosphere calculations fully specify the mixing of polarization at the mode collapse points ($\omega_{\pm}, \theta_{\pm}$). Ho & Lai (2002) have pursued calculations invoking the two extreme limits of “no collapse” and of wholesale exchange of polarization identities through all photon trajectories, with the correct solution presumably intermediate to these extremes; these authors have since drawn conclusions similar to those above which favor the limit of distinct polarization modes (Ho & Lai 2003). From the preceding discussion, it is acceptable to assume that mode-collapse will have at best a modest effect on the emergent NS spectrum regardless of the magnitude of the effect within the θ_- annulus, and we consider only the non-collapse limit in the remainder of this article. The mode ambiguity is related to the breakdown of the Faraday depolarizing limit, and a more exacting solution will likely require radiative transport of the full Stokes vector, and careful treatment of the anti-hermitian components of the plasma dielectric.

3 RADIATIVE TRANSFER AND NEUTRON STAR ATMOSPHERES

The fundamental parameters of the model atmosphere are the surface gravity g_s , the total flux propagating through the atmosphere \mathcal{F}_{cons} , the magnetic field strength and orientation \vec{B} , and the plasma composition. For a given equation of state, these parameters uniquely specify the model.

The surface gravity of a relativistic star is

$$g_s \equiv \gamma \frac{GM}{R^2} = \frac{GM/R^2}{\sqrt{1 - 2GM/R}}$$

and for M, R characteristic of NSs, $g_s \sim \mathcal{O}(10^{14}) \text{ cm s}^{-2}$. The large surface gravity gives an atmospheric scale height $d \ll R$, and gradients in the gravitational and magnetic fields of the star may be neglected for the purpose of calculating the atmospheric structure. The thin plasma atmosphere is well described by a semi-infinite plane parallel geometry. We do not consider extended atmospheres or those with bulk motions.

In the absence of heat sources or sinks, the total energy flux is a conserved property, and we define the effective temperature T_{eff} in terms of this conserved flux:

$$\sigma_{SB} T_{eff}^4 = \mathcal{F}_{cons}$$

for σ_{SB} the Stefan-Boltzmann constant. Conductive transport at densities characteristic of NS atmospheres ($\rho \sim 0.1 - 10 \text{ g cm}^{-3}$) is inefficient compared to radiative diffusion, while convective instabilities, already suppressed in the limit of complete ionization, are further inhibited by Ohmic dissipation in strong magnetic fields. Consequently, neither conductive nor convective transport is included in our calculations.

In a semi-infinite, plane parallel geometry, the steady-state transport of radiation in mode j for photon momentum \mathbf{k} at any particular depth in the stellar medium is described by the differential equation

$$\mu \frac{dI_{\nu}^j(\mathbf{k})}{dm} = \chi_{\nu}^j(\mathbf{k}) I_{\nu}^j(\mathbf{k}) - \eta_{\nu}^j(\mathbf{k}) \quad (34)$$

The momentum vector \mathbf{k} is assumed to be outward pointing, and is specified by the surface latitude $\mu = \cos \theta_k$ and azimuthal angle ϕ ; the latter is measured with respect to a reference direction to be defined later. All functional dependence on the magnetic field vector

is subsumed in the formulation of $\chi_\nu^j(\mathbf{k})$ and $\eta_\nu^j(\mathbf{k})$. It is advantageous to write the radiative transfer equation (34) under transformation to the pair of conjugate intensity (Feautrier) variables:

$$u_\nu^j(\mathbf{k}) = \frac{1}{2} [I_\nu^j(\mathbf{k}) + I_\nu^j(-\mathbf{k})] \quad (35)$$

$$v_\nu^j(\mathbf{k}) = \frac{1}{2} [I_\nu^j(\mathbf{k}) - I_\nu^j(-\mathbf{k})] \quad (36)$$

where for $\mathbf{k} = \mathbf{k}(\mu, \phi)$, $-\mathbf{k} = \mathbf{k}(-\mu, \pi - \phi)$ and $\mu > 0$. The transfer equations in these variables are

$$\mu \frac{dv_\nu^j(\mathbf{k})}{dm} = \chi_\nu^j(\mathbf{k}) u_\nu^j(\mathbf{k}) - \eta_\nu^j(\mathbf{k}) \quad (37)$$

$$\mu \frac{du_\nu^j(\mathbf{k})}{dm} = \chi_\nu^j(\mathbf{k}) v_\nu^j(\mathbf{k}) \quad (38)$$

where we have relied on the residual symmetry of the plasma emissivity about the magnetic field orientation, i.e. $\eta_\nu^j(\mathbf{k}) = \eta_\nu^j(-\mathbf{k})$. Following the usual Feautrier development, we obtain the transfer equations for the surface boundary, intermediate depth, and lower boundary, respectively:

$$\mu \chi_{j,\nu}^{-1} \frac{du_\nu^j}{dm} = u_\nu^j - I_\nu^j(-\mathbf{k}) \quad (39)$$

$$\mu^2 \frac{d}{dm} \left(\chi_{j,\nu}^{-1} \frac{du_\nu^j}{dm} \right) = \chi_\nu^j u_\nu^j - \eta_\nu^j \quad (40)$$

$$\frac{du_\nu^j}{dm} = \frac{3}{16} \frac{\mathcal{F}_{cons}}{T^3} \chi_R \frac{dB_\nu}{dT} \quad (41)$$

for the Rosseland mean opacity:

$$\frac{1}{\chi_R} = \frac{\pi}{4\sigma_S B T^3} \int \left(\sum_{j=1}^2 \frac{1}{\chi_\nu^j} \right) \frac{dB_\nu}{dT} d\nu \quad (42)$$

At the stellar surface, the term $I_\nu^j(-\mathbf{k})$ can be used to quantify either the intensity in mode j of the incident radiation field of an externally illuminated atmosphere, or a small correction to the intensity field to account for the finite optical depth of the surface stratum in a numerical calculation ($0 < \tau_\nu^j \ll 1$). For our present discussion, we will set $I_\nu^j(-\mathbf{k}) = 0$.

The large optical depth in either mode to the boundary allows for ample redistribution of the flux by (principally) thermal absorption and reemission; in magnetized models, the boundary flux of (41) can be arbitrarily distributed in the two modes with no effect on the result of the radiative transfer. In strongly magnetized plasma, the opacity introduces an additional non-trivial angular dependence to χ_R in (41), neglected at the lower boundary but otherwise accounted for in the RTEs at all other depths. The anisotropy ultimately has no appreciable effect on the emergent radiation field, owing to the tremendous optical depth to the lower boundary (typically $\tau > 10^2$), and the plasma can be modeled as isotropic with no effect to the emergent spectrum.

3.1 Radiative equilibrium

The total flux gradient is found by integration of the transfer equation (34) over all frequencies and angles where the opacity and emissivity have been expanded into their respective thermal and scattering contributions. Using the definition of the (coherent) scattering emissivity $j_{i,\nu}^{sc}$, and demanding that the flux be invariant with depth, this is

$$\int_0^\infty d\nu \int_{+\Omega} d\Omega \left[\sum_{j=1}^2 (\alpha_\nu^j u_\nu^j - j_{j,\nu}^{th}) \right] = 0 \quad (43)$$

Equation (43) is a necessary condition for radiative equilibrium, but is not by itself sufficient to constrain the *magnitude* of the flux — the thermal balance prescribed here does not relate continuous variations in flux with depth. When simultaneously integrated with the system of radiative transfer equations (RTEs), where the total conserved flux is specified in the depth boundary (41), equation (43) provides a robust constraint. To directly calculate the flux \mathcal{F}_ν , we evaluate the conjugate field $v_{\mu\nu}^j$ from either the Feautrier definitions at the surface or from eqn (38) at any other depth:

$$\mathcal{F}_\nu = 2 \int_0^{2\pi} \int_0^1 \mu \sum_{j=1}^2 v_{\mu\nu}^j d\mu d\phi \quad (44)$$

3.2 Hydrostatic equilibrium

Our model of the neutron star atmosphere will neglect bulk motion of the plasma, and will therefore assume a hydrostatic structure. The total pressure at any depth of the atmosphere is the sum of contributions from the ideal gas pressure, the radiation field, and non-ideal effects owing to interactions between plasma constituents:

$$P = P_{ideal} + P_{non-ideal} + P_{rad} \quad (45)$$

The ideal gas pressure, including electron degeneracy, is

$$P_{ideal} = NkT + n_e(y_p - 1)kT \quad (46)$$

where N is the total number density of the plasma constituents, and the parameter y_p is the ratio of Fermi integrals $I_p(\alpha)$, $y_p = I_p/(pI_{p-1})$. For unmagnetized plasma, $p = 3/2$, and in quantizing magnetic fields, $p = 1/2$. The electron density is an independent model variable in our calculation; to ensure a self-consistent equation of state, we compare the value of n_e of the current iterate to that given by (Clayton 1983; Potekhin et al. 1999)

$$n_e = \begin{cases} \frac{4}{\sqrt{\pi}\lambda_e^3} I_{1/2} & \ell > 1 \\ \frac{1}{\sqrt{\pi}\lambda_e} \left(\frac{eB}{hc} \right) I_{-1/2} & \ell \lesssim 1 \end{cases} \quad (47)$$

where $\lambda_e = (2\pi\beta\hbar^2/m_e kT)^{1/2}$ is the electron thermal wavelength, and the parameter ℓ is defined in (30). The electron degeneracy parameter α is evaluated from n_e either by inversion of the Fermi integral (Antia 1993) or by a numerical root search, from which the degeneracy pressure is calculated. In strongly quantizing magnetic fields, the phase space volume occupied by the electron distribution is much smaller than that of a weakly magnetized plasma, tempering the onset of degeneracy which occurs at higher densities than for unmagnetized plasma. At intermediate magnetic field strengths, the degeneracy contribution to the gas pressure should be evaluated by a sum over occupied Landau states. In practice, degeneracy pressure contributes less than $\sim 4\%$ at even the deepest model strata, and has no discernible influence on the emergent spectrum. In our models the degeneracy pressure at finite $B \lesssim 10^{10}$ G is approximated by the zero field limit.

Non-ideal contributions to the pressure include the Coulomb interaction of the ionized plasma and, for an incompletely ionized plasma, the atom-atom and atom-ion interactions in the neutral plasma component. The latter are neglected in our simplified EOS; for the former, we use the Debye-Hückel approximation in both magnetized and unmagnetized plasma (Clayton 1983):

$$P_{Coul} = -\frac{2e^3}{3} \left(\frac{2\pi}{kT} \right)^{1/2} (\xi n_e)^{3/2} \quad (48)$$

where ξ is a compositional parameter $\mathcal{O}(1)$. This approximation breaks down when the Coulomb energy at the mean electron-ion

separation becomes comparable to the local thermal energy, which can occur at depth in models which are both strongly magnetized and very cool.

The radiation pressure is formally a tensor quantity but usually taken to be isotropic in conventional atmosphere models. Finite anisotropies to the pressure tensor are induced in oblique magnetic fields; however, as we shall see from the discussion of model results, the radiation force plays only a minor role in the total pressure structure of the neutron star atmosphere (this is especially true in the region of photon decoupling) and we will consider only the $\hat{z}\hat{z}$ component of the pressure tensor regardless of field orientation in these calculations. In CGS units this scalar pressure is:

$$P_{rad} = \frac{4\pi}{c} \int_0^\infty d\nu \int_{+\Omega} d\Omega \mu^2 \sum_{j=1}^2 u_{\mu\nu}^j \quad (49)$$

The fiducial depth in our atmosphere model is the Lagrange variable m (g cm^{-2}), in terms of which the total pressure gradient is:

$$\frac{dP}{dm} = g_s \quad (50)$$

Eqn (50) is to be integrated simultaneously with the RTE system and other constraints. In the limit of $m_0 \rightarrow 0$ the total pressure will equal that of the emergent radiation field; in numerical calculations it is not possible to realize this limit, and the pressure $P(m_0)$ will retain finite contributions from each source, dominated by the gas pressure P_g . At the surface, we require $P(m_0) = g_s m_0$.

Finally, the system of equations is closed by the EOS. In the limit of complete ionization, the statistical equilibrium for a light element plasma is particularly simple: we require only that the local charge distribution of the model be neutral, and that particle number be conserved everywhere:

$$n_e = \sum_{s \neq e} Z_s n_s, \quad N = \sum_s n_s$$

Although convective transport is neglected in our prescription for energy transport and flux conservation in the stellar atmosphere, conditions amenable to convection may arise in the resultant atmospheric structure, and the validity of our non-convective model hypothesis should be evaluated in the final result. The onset of convective instability is estimated by the Schwarzschild criterion, generalized to include the effects of radiation pressure, and of the neutral species gradient in unmagnetized atmospheres:

$$\nabla_R \equiv \left(\frac{d \ln T}{d \ln P} \right)_R > \left(\frac{d \ln T}{d \ln P} \right)_A \equiv \nabla_A \quad (51)$$

The radiative gradient ∇_R is evaluated from the model $T(P)$ by numeric differentiation and ∇_A is calculated as described by Krishna-Swamy (1961). This measure of the adiabatic gradient does not include the effect of Ohmic dissipation in magnetized plasma, which tends to improve the stability of the plasma against the onset of convection. None of the models presented in §5 show evidence of convective instability; Zavlin et al. (1996a) find that convection occurs in light element atmospheres only for exceptionally cool models, $T_{eff} \lesssim 5 \times 10^4$ K.

4 SOLUTION TECHNIQUE

Apart from the strategy used to refine the model, successful convergence will often depend critically upon the properties of the trial or

seed solution, and on the distribution of points on the discrete grids over continuous model dimensions, e.g. energy, angle and depth.

4.1 Seed thermal structure

We use a power-law prescription for the plasma conductivity assuming free-free absorption is the dominant source of opacity, i.e. the Kramers opacity (Clayton 1983). This simplified model has two functions: first, to suggest reasonable bounds for the depth variable m which will cover the range of photospheric depth for a prescribed range of photon energies; and second, to construct an initial temperature profile which crudely approximates radiative equilibrium. Derivations of the mass, temperature and optical depth relations for this model proceed from the discussion in Heyl & Hernquist (1998a).

For the monochromatic optical depth τ to photons of energy E (keV), the equivalent mass column density (g cm^{-2}) in this model is given by

$$m_E(\tau) = 2.74 \times 10^{-2} T_{eff}^{3/7} (E^3 \tau)^{17/28} (\mu g_{s,14})^{-1/2} \quad (52)$$

Here, $g_{s,14} \equiv g_s/10^{14}$ and μ is the mean molecular weight of the plasma, which can be defined in some average sense for H/He mixtures with compositional gradients. The required depth range is therefore approximately bounded by the range of photon energies considered in the model. For the NS spectra under consideration, we take for this energy range $10^{-3} - 10$ keV. The Kramers model underestimates the surface temperature of the converged result, and generally overestimates the opacity of the plasma in the outermost strata. Consequently, it is sufficient to define the surface boundary by evaluating (52) for the lowest model energy at $\tau = 0.01$, and the lower boundary by evaluating (52) for the highest model energy at $\tau = 1.0$. For models with $\log B \geq 11.0$ the lower depth boundary is multiplied by $B_{11} \equiv B/10^{11} \text{G}$ to account for the reduced opacity at X-ray energies in the extraordinary polarization mode. The total optical depth range for a converged model is typically $\tau \sim 10^{-5} - 10^5$. The temperature profile derived from the power-law model is

$$T(m) \simeq 56 (\mu g_s T_{eff}^4 m^2)^{2/17} \quad (53)$$

The initial density profiles can be approximated by assuming only ideal gas pressure contributes to the total.

4.2 Mesh generation

The rate and quality of model convergence for a particular choice of parameters are sensitive to the choice of discretization of the continuous model dimensions, and will often require the careful distribution of grid points in depth m , photon energies E and trajectories through the plasma (μ, ϕ) . The current numerical implementation requires the angle-energy mesh to remain fixed during the calculation. We expect that a reliable solution should result from a mesh which is designed to capture significant features of the plasma opacity with respect to these dimensions.

4.2.1 Frequency mesh

For most NS spectra we consider the energy range $E = 10^{-3} - 10$ keV which provides sufficient coverage of the spectrum from optical through soft X-ray energies for a broad range of T_{eff} . The continuum frequency mesh is allocated by dividing the total energy range into logarithmic subintervals, each populated with equal

numbers of mesh points. Any of these intervals may be further subdivided to accommodate an atomic or cyclotron feature, in which case the continuum interval is split into smaller intervals with mesh point densities proportional to their widths. We typically use 6 – 8 points per $\log E$ to describe the continuum, with an additional $NC = 4 - 8$ points cast in each cyclotron resonance.

4.2.2 Angle mesh

Several strategies for prescribing the angle mesh may be considered, and we take advantage of symmetries about the magnetic field when available. The radiative transfer equations in terms of the conjugate Feautrier variables require definition of the outgoing photon trajectories $\mu = (0 - 1]$.

For weakly magnetized plasma ($\log B \lesssim 10$), the anisotropy imposed on the emergent radiation field is mild at X-ray energies. In this nearly isotropic plasma, we adopt a simple Gauss-Legendre or Gauss-Radau distribution in the viewing latitude μ ; the latter distribution is constructed by holding the $\mu = 1$ node fixed in the Legendre polynomial. Model results calculated in the isotropic limit which include the normal LOS do not differ substantially from those where this trajectory is excluded. In this regime, as few as 5 points can be used to describe the angular intensity distribution.

Departures from the isotropic plasma response affect the X-ray spectra when $\log B \gtrsim 10$, where large variations in the angular dependence of the opacity allow for photon decoupling from broad range of plasma temperature. For $u_e \gtrsim 5.3$ the geometric factor G_X acquires a maximum at θ_p roughly delineating a bimodal angular distribution of radiation: a pencil beam component directed along the magnetic field lines, and a broader fan component at more oblique angles. The angular width of the pencil component declines with increasing u_e after achieving a maximum near $u_e \simeq 11$; resonances in the polarization vectors (ionic or vacuum) also have large opening angles, but the pencil beam transports little flux in NS models with $B \gtrsim 10^{13}$ G. It is desirable to prescribe a fixed angle distribution which samples the dependence across the entire spectrum of model energies for a given magnetic field strength, and which emphasizes the transition between the two components. These *pencil weighted* schemes distribute mesh points on intervals of $\log(1 - \mu)$ where $(1 - \mu)_{min}$ is generally 10^{-4} . Good resolution of the pencil and fan emission components can be achieved with as few as 10-16 points. As in the isotropic case, the normal sighting can be included as desired.

Oblique fields & the azimuthal mesh — For normal magnetic field vectors, the radiation field is azimuthally symmetric models and degenerate in the ϕ dimension; for this, we use a single mesh point at $\cos \phi = 1$. Weakly magnetized models can also be computed with sufficient accuracy in this approximation. Oblique magnetic fields $B \gtrsim 10^{10}$ G clearly break the azimuthal symmetry and for generally oblique magnetic field inclinations we are obliged to consider $\phi : 0 - \pi/2$ with emphasis on the pencil width about the field axis ($\theta_b, \phi = 0$). When $\theta_b = \pi/2$, the plasma response recovers partial symmetry, and the calculation can be restricted to $\phi : 0 - \pi/4$, with the remainder of the plane mapping into this range. The direction $\phi = 0$ is defined by the projection of the (oblique) magnetic field vector onto the plane of the atmosphere ($\vec{x} = \hat{b} - \hat{n} \cos \theta_b$). For generally oblique magnetic fields, we use 5 – 8 azimuth points in the following overlapping distributions: (i) two nodes are assigned at $\cos \phi = -1, 1$ and (ii) the remainder distributed logarithmically in the quadrant $\cos \phi = [0, 1]$ similarly to the pencil weighted scheme described above. Fully orthogonal models ($b = \pi/2$) can be calculated with as few as 4 azimuthal

points, and for these we choose a Gauss-Lobatto distribution with anchored nodes at $\cos \phi = [0, 1]$. Regardless of their distribution, we calculate the angle the trajectory and the magnetic field for each angle pair (μ, ϕ) :

$$\cos \theta_{bk} = \cos \phi (\sin \theta_b \sin \theta_k + \cos \theta_b) \quad (54)$$

for use when evaluating the geometric corrections to the plasma opacity detailed in §2. Model results are invariant under reversal of the field direction.

4.2.3 Depth mesh

In general, we compute the atmosphere models on a fixed depth mesh with 10 points per decade for a total of 90 – 130 points. Models including a strong magnetic field, with non-trivial vacuum contributions to the opacity, often require special care; experience has shown that these models benefit from an additional depth mesh component which adaptively traces the coupling of density with photon energy near the vacuum resonance (e.g. eqn (31), see also Ho & Lai (2003)). These adaptive depth points are found by interpolating the current density profile n_e to find the critical density for vacuum resonance formation at each model energy from (31), and ignoring photon energies which do not see the resonance on the current range of n_e described by the model. A single adaptive point is assigned to the “core” of the vacuum resonance; additional points can be symmetrically distributed at $\rho_{res}(1 \pm n\epsilon)$, $n = 1, 2 \dots$, for $\epsilon \ll 1$ but this is not required. All independent model variables (T, n, u) are then interpolated for each adaptive depth point from the current model solution. In successive iterates, the previous adaptive mesh is discarded after interpolation of the current iterate’s adaptive points.

4.3 Formal radiative transfer calculation

For a given atmospheric structure $T(m), n_s(m)$ we calculate the opacities and thermal emissivities at each strata of the model. The radiative transfer equations (39-41) are transcribed to a simple differencing scheme; the discretized RTE at intermediate depth for radiation of a particular energy, mode and trajectory (with these indices suppressed) is:

$$-\mu^2 D_- u_{d-1} + [\mu^2 (D_- + D_+) + \overline{\Delta m} \chi] u_d - \mu^2 D_+ u_{d+1} = \overline{\Delta m} (\eta^{th} + \eta^{sc}) \quad (55)$$

and the surface and depth boundary equations are

$$\begin{aligned} -\frac{\mu^2}{2} D_+ u_2 + \left[\frac{\mu^2}{2} D_+ + \mu + \frac{1}{2} \Delta m_+ \chi \right] u_1 \\ = \mu I^- + \frac{1}{2} \Delta m_+ (\eta^{th} + \eta^{sc}) \\ -\frac{\mu^2}{2} D_- u_{ND-1} + \left[\frac{\mu^2}{2} D_- + \frac{1}{2} \Delta m_- \chi \right] u_{ND} \\ = 3\mu^2 \frac{T_e^4}{16} \chi^{-1} \chi_R \frac{dB}{dT} T^{-3} + \frac{1}{2} \Delta m_- (\eta^{th} + \eta^{sc}) \end{aligned} \quad (56)$$

for $d = 2 \dots ND - 1$. The differenced boundary equations (56-57) have been promoted to second order accuracy by substitution of (40); higher order accuracy can be obtained by evaluating the gradient of the emissivity (Auer 1976), but does not substantially improve our results. The depth intervals are $\Delta m_{\pm} = |m_{d\pm 1} - m_d|$, $\overline{\Delta m} \equiv \Delta m_+ + \Delta m_-$ and the differencing coefficients D are (Auer et al. 1977):

$$D_{\pm} \equiv \frac{(\chi_{d\pm 1}^{-1} + \chi_d^{-1})}{\Delta m_{\pm}}$$

The scattering integrals are expanded as a sum over incoming photon modes and trajectories which explicitly couples radiation in the two polarizations states, and integrates the scattering emissivity *in-situ*:

$$\eta_i^{sc}(k) = \frac{n_e}{\rho} \sum_{k'} w_{k'} \sum_{j=1}^2 u^j(k') \left(\frac{d\sigma_{ji}^{k'k}}{d\Omega'} \right)$$

The angular integration weights w_k are the product of the respective μ and ϕ Gaussian weights corresponding to the trajectories k . Rendering integrations of the total opacity and emissivities on the fixed angle mesh accurately preserves both thermal balance and the conservative scattering processes.

For a particular model energy E , the coefficients of the vector $u_{d,E} = (u_1^j \dots u_{NA}^j)_{d,E}$ from (55-57) are written into matrix coefficients

$$-A_{d,E} u_{d-1,E} + B_{d,E} u_{d,E} - C_{d,E} u_{d+1,E} = K_{d,E} \quad (58)$$

which are generally full but diagonally dominant; the K_d are the thermal emissivity factors and boundary terms from eqns (56) and (57). For coherent scattering, radiation streams of different energies are not coupled and, per frequency, the RTE system is simply expressed in this block tridiagonal form for mode-trajectory pairs organized by depth which can be solved by standard elimination techniques. Matrix inverses are never explicitly evaluated – instead the common matrix terms in the projection operators are *LU* factored and the intermediate vectors and matrix operators then found by back-substitution. All algebraic reductions in our code are made using standard *BLAS* and *LAPACK* routines.

The resultant radiation field, while consistent with the prescribed atmospheric structure, cannot be expected to satisfy flux conservation. The trial solution will therefore be iteratively refined by deducing corrections to each model variable such that the entire system of RTEs and constraints are driven towards a convergent solution. This proceeds by complete linearization (CL).

4.4 CL algebra

The tridiagonal organization of the formal RTE system in the previous section provides the algebraic basis for extension to the full iterative problem in the complete-linearization technique (Auer & Mihalas 1969), although the detailed organization of the coefficients is distinct from that of the formal transfer calculation. The constrained RTE system is again transcribed to a numeric grid in a simple differencing scheme, but now *linear perturbations* to the radiation components and physical fields are the independent model variables. The correction to any model variable will be associated with a linearized equation: either an RTE (for u) or constraint (for T, N, n_s). The solution is represented by the vector $\vec{\Psi} = (\Psi_1 \dots \Psi_D)$, where $\Psi_d = (N, T, n_s, u_{\mu\nu}^j)_d$ are formed from the current model state. Corrections to the model solution are found by solving an equation of the form $O\delta\vec{\Psi} = E$ where E is the error in the current solution, and O is an operator derived from coefficients of the perturbed equations. For brevity we sketch the main elements of the technique; see Mihalas (1978) for a complete example of complete linearization applied to a simple atmosphere.

In each model equation, the independent variables are replaced by first order corrections, $T \rightarrow T + \delta T$, etc. Functions are linearized by taking partial derivatives with respect to the independent model variables:

$$\chi \rightarrow \chi + \frac{\partial \chi}{\partial T} \delta T + \sum_s \frac{\partial \chi}{\partial n_s} \delta n_s \quad (59)$$

and similarly for the emissivities η^{th} and η^{sc} . The efficiency of the CL cycle is diminished by properties held constant during the iteration, therefore differentiation like that in (59) includes partials taken with respect to the squared polarization components and the Gaunt factors. All derivatives in the model are evaluated analytically at the current values of the model variables; for numerical work these are most conveniently expressed in logarithmic form. Upon substitution of all model variables, the linearized equations are reorganized by collecting terms from the unperturbed equations to form the error E , while coefficients of each model variable correction are grouped by depth. The CL coefficients of the constrained system of equations are written into matrix coefficients

$$-A_d \delta \Psi_{d-1} + B_d \delta \Psi_d - C_d \delta \Psi_{d+1} = E_d \quad (60)$$

where the matrix coefficients A, B, C now contain the full spectrum of differencing coefficients, integration weights and constants of the linearized RTE system and its constraints per depth, and E_d is the error vector whose components are given by the difference between the RTEs (constraints) for $u(N, T, n_s)$ and the exact solution calculated from the current model state. Coefficients of the j th variable at depth $d-1$ in the i th equation at depth d are written into the $A_{d,ij}$ etc. The entire system forms a block tridiagonal matrix which is solved by *LU* factorization and substitution. The new model state is found by updating each model variable with its linear corrections, and the system is iteratively corrected in this fashion until the root vector is rendered within some prescribed tolerance to be described below. This procedure is multivariate Newton-Raphson iteration. Note that information (model corrections) from a given stratum propagate over the mean free path of the radiation field via the transfer equations, and model convergence is global.

CL often over-steps the convergent solution in early stages of the computation, and we limit the magnitude of the temperature corrections to $|\Delta T/T| \leq (0.4 - 0.7)$ to prevent model variables from acquiring non-physical values from “rogue” iterates. When this condition is engaged at any depth, corrections to all other fields are discarded, the density made consistent with g_s and the correction-limited $T(m)$ as in §4.1, followed by a formal recalculation of the radiation field (§4.3). The typical CL cycle is summarized by (1) allocation of mesh points in all model dimensions, either from command-line arguments to the program, or through defaults; (2) this is followed by tabulation of the Gaunt factors and their temperature derivatives for each model photon energy in magnetized models, over a range of temperature $\log T_{eff} \pm 1.5$; (3) calculation of the trial thermal structure $T(m), n_s(m)$, and the run of opacity χ_ν^j and emissivity η_ν^j with depth for all photon trajectories θ_{bk} in each mode; (4) a formal calculation of the radiation field from these opacities (§4.3); followed by (5) the CL iterates. We adopt as acceptable convergence criteria that $\Delta T/T < 10^{-3}$ and $\Delta F/F_{cons} < 10^{-3}$ at all depths. These limits are achieved in 5-13 iterates for typical choices of computational grid densities and dimensions, while the convergence rate can become superlinear in the final iterates.

5 MODEL RESULTS

We have implemented the methodology of §4 in an efficient stellar atmosphere code, and computed model atmospheres and spectra for a range of parameters consistent with measured and inferred

properties of cooling, isolated NS. We consider stars with surface magnetic fields up to 10^{14} G, and assume an ionized Hydrogen plasma photosphere described by the opacities formulated in §2. For weak and intermediate field strengths, we consider the range $5.5 \leq \log T_{\text{eff}} \leq 6.5$, while for the magnetar case we consider only $6.2 \leq \log T_{\text{eff}} \leq 6.7$. We restrict our discussion to models with surface gravity $\log g_s = 14.38$, corresponding to NS of canonical mass $M = 1.4 M_\odot$ and radius $R = 10$ km. Spectra are illustrated in the stellar surface frame and must be redshifted by $z = 0.306$ to describe the flux measured by a distant observer. All results are derived from models converged to the tolerance described in §4.4. No smoothing is applied to figures derived from converged model results.

The principal energy scaling of the geometric corrections $G_i(k)$ and $G_i^{\text{ff}}(k)$ enter through the magnetic field strength in the ratio $u_e = (\omega_{c,e}/\omega)^2$, and it is natural to organize our discussion of model results by ranges of B . This grouping emphasizes the discriminatory properties of the stellar spectra, but also naturally collects results appropriate for comparison to different classes of observed sources (quiescent X-ray binaries, radio pulsars, anomalous X-ray pulsars). The selection of models presented in this discussion, while not exhaustive, is representative of typical values for observed manifestations of NS thermal X-ray emission.

X-ray polarimetry is a potentially predictive measure of the surface properties of cooling NS, but is of immediate interest only for relating the model input physics to the theoretical spectra. In our present study, it is adequate to define the net polarization $\Pi(E)$ in terms of the partial flux in each polarization mode (44):

$$\Pi(E) = \frac{\mathcal{F}^X(E) - \mathcal{F}^O(E)}{\mathcal{F}^X(E) + \mathcal{F}^O(E)}$$

The flux input to the model (41) can have arbitrary polarization content; the radiation field is efficiently redistributed by absorption and scattering processes and the final spectrum is independent of the input polarization fraction provided $\tau_E^{\text{base}} \gg 1$. The polarization content of the *intensities* at large depth is essentially zero, and that of the final emergent spectrum is determined by the relative temperatures at which the two modes decouple from the atmosphere. Upon decoupling from the plasma, the intensity and its angular distribution (i.e. flux and pressure) in either mode asymptotically acquire values which are unchanging in the higher strata. As the gas pressure declines toward the atmospheric boundary, the radiation pressure assumes the dominant role; exterior to the star, the pressure is entirely that of the radiation field. All model calculations described here account for the radiation pressure, but throughout the range of photon decoupling its contribution to the total P is negligible.

5.1 Unmagnetized models ($B \lesssim 10^{10}$ G)

The onset of magnetic corrections to the plasma opacity occurs where $u_e \simeq 1$, and the electron cyclotron feature clearly delineates the polarizing properties of the magnetized plasma. Consequently, the X-ray spectra of magnetized NS atmospheres having $B \lesssim 10^{10}$ G are essentially indistinguishable from the zero-field case for the same plasma composition and total flux, and may be classified as *unmagnetized* models. The transition from classical to quantizing magnetic field occurs within the range of T_{eff} described for $B = 10^9 - 10^{10}$ G. As described in §2 our calculation of the bremsstrahlung Gaunt factor is somewhat inaccurate for $\ell \sim 1$, and here we will assume the zero-field g for each effective temperature at these field strengths. Consequently, the polarization properties

derived for models in this regime are influenced only by the normal mode vector decomposition, but permit comparison between models at different T_{eff} having the same field strength and guarantee consistent calculation of g at all strata of a given model. In Figure 1, we compare spectra calculated in the weak field regime for a range of T_{eff} and find no magnetic field dependence for the emission $E \gtrsim 0.2$ keV. For the range of T_{eff} considered here, the spectra in the unmagnetized field regime satisfy a linear relation between the peak spectral energy the effective temperature similar to the Wien displacement of the Planck function; $E_{\text{peak}} \simeq 4.7kT_{\text{eff}}$ in these unmagnetized models.

Departures from the zero field results at optical and UV wavelengths for finite B arise from the redistribution of resonantly absorbed radiation to longer wavelengths in accordance with flux constancy in radiative equilibrium. The magnitude of this redistribution is greater where the cyclotron line is approximately coincident with the peak thermal emission (e.g. $\log T_{\text{eff}} = 5.6$ at 10^{10} G) owing to both the scaling of the effective cyclotron line width and because there is more radiation in the spectral peak which can be reprocessed. Additional details of the influence of cyclotron energy redistribution on visual magnitudes are presented elsewhere (Lloyd et al. 2003). More generally, photons absorbed in a neutral plasma component is likewise reemitted at longer wavelengths in radiative equilibrium producing enhanced emission below the absorption feature.

Only X mode radiation is resonantly absorbed in the electron cyclotron line, and the excess ordinary mode contribution yields a large net polarization in the resonance. The effective width of the cyclotron feature is approximately scale invariant. At optical and near UV wavelengths the X mode photosphere is displaced to higher temperatures, owing to the reduced opacity in this mode. The spectrum is largely unpolarized at energies $\omega \gg \omega_{c,e}$, for which the opacity reverts to the anticipated unmagnetized result, although, as the magnetic field strength approaches 10^{10} G ($\hbar\omega_{c,e} \simeq 0.12$ keV), the unpolarized limit is recovered only gradually at high energies. For energies $E \gtrsim 2.5$ keV, the photosphere temperature is saturated at $T \sim 2 \times 10^6$ K where (frequency independent) electron scattering is the principal opacity source. The polarized spectra and plasma decoupling properties of the 10^{10} G models are illustrated for several T_{eff} in Figs. 2 and 3. The decoupling density $\rho(\tau_E) = 1$ in each mode is approximately independent of flux temperature for a given value of B . Collective phenomena become significant in the plasma response at long wavelengths, are not fully described by the opacity formulated of §2 – this limitation can be seen at optical frequencies in the 10^{10} G models where photons decouple at $v_e \simeq 1$ (Fig. 3).

Radiative equilibrium mitigates the influence of cyclotron absorption by adjusting the asymptotic surface structure $T(m)$. Figure 4 demonstrates the magnitude of this effect for two values of T_{eff} . The ordering of surface temperature $T(m_0)$ with magnetic field differs for each value of T_{eff} , and the departure from the unmagnetized temperature profile at finite B occurs at greater depth with increasing magnetic field. At depth where only photons with $\omega > \omega_{c,e}$ decouple, the models have identical thermal structure. Radiation emerging from this isotropic plasma has an angular distribution characteristic of limb-darkening, which is preserved for oblique magnetic fields of modest strength.

5.2 Intermediate fields ($10^{11} \lesssim B \lesssim 10^{13}$ G)

In the unmagnetized plasma regime, geometric corrections to the opacity are both weak in amplitude, and nearly independent of

propagation angle; consequently, high energy emission in weakly magnetized models is well described by the equivalent zero field results. Departures from isotropic plasma response are prominent in the X-ray spectra of models with $10^{11} \lesssim B \lesssim 10^{13}$ G comparable e.g. to the radio pulsars (RPs) where they are manifest in the finite polarization $\Pi(E)$ of the spectrum and in the angular distribution of intensities. Polarization of the thermal radiation is essentially complete for $B \gtrsim 10^{12}$ G, and the spectral envelopes of these models differ substantially from their weakly magnetized counterparts, owing to the harder energy dependence of the X mode opacity ($\propto \nu^{-1}$) which suppresses the amplitude of emission in the high energy tail and shifts the peak emission energy to lower frequencies. Inflections in the equilibrium thermal structure (Fig. 7) are related to displacement of X mode decoupling to deeper, hotter strata than for the ordinary mode. In this regime, the asymptotic surface temperature declines for increasing B owing to the reduced energy density in the O mode field. The peak energy displacement with effective temperature is $E_{peak} \simeq 4.0kT_{eff}$, and the spectrum is dominated by radiation component in the X mode field. Vacuum corrections to the plasma dielectric are negligible in these models.

The proton cyclotron resonance enters the optical regime at $\log B \simeq 11.5$, and soft X-rays at $B \simeq 10^{13}$ G. The apparent depth of the feature is greater than that of the electron feature seen in weakly magnetized models owing to the overall depletion of O mode intensity at $\omega < \omega_{c,e}$. The proton line width scales with the cyclotron frequency similar to that of the electron resonance (Fig. 6). Collective phenomena play an increasingly important role at long wavelengths in these models, and the energy below which the plasma attenuation becomes significant is $E_{plas} \simeq 0.5 \log B - 7.6$. At these long wavelengths the specific photosphere is coincident with the boundary v_e owing to the large optical depth accumulated at this boundary. The broad electron resonance $E \sim 11.6$ keV for models of 10^{12} G is not resolved in these calculations, though its influence is obvious in the polarized spectra in Figures 5-6.

The angular intensity distributions in the intermediate field regime acquire a pronounced pencil beam component oriented with the magnetic field vector. The pencil is essentially unpolarized due to the degenerate opacity for $\theta_b \simeq 0$ but acquires large net polarization away from this trajectory. The amplitude of the pencil component declines with increasing magnetic field inclination due to previously mentioned limb effects, but the pencil width is approximately independent of inclination (Fig. 8). The O mode opacity is not magnetically depressed outside the pencil and the intensity profile acquires a highly polarized fan-like profile dominated by X mode emission (Fig. 9). Despite the large intensity in the pencil, less than 10% of the total flux is transported in this component at 10^{12} G; and by 10^{13} G, less than 1% is emitted in the pencil. In general, the O mode flux contribution declines with increasing field inclination b , as does the total emission in the high energy tail (Fig. 10).

5.3 Intense field limit ($B \simeq 10^{14}$ G)

The abrupt X mode opacity variation induced by vacuum polarization plays a crucial role in the equilibrium thermal structure and spectral properties of ultramagnetized plasma atmospheres ($B \gtrsim 10^{14}$ G). The magnetic suppression of the X mode opacities is greater in this regime than for the RPs, and O mode intensities contribute $\lesssim 1\%$ of the total flux. Strictly, the precise polarization content of the radiation field is indeterminate in the normal-mode analysis as radiation propagates from the plasma dominated regime, through the resonance into the vacuum dominated regime.

The shape of the spectral envelope is substantially affected by both direct absorption within the opaque layer, and its indirect influence on the equilibrium thermal structure. The displacement rules described for $B \lesssim 10^{13}$ G is ambiguous for 10^{14} G owing to spectral reshaping through vacuum effects. The pencil component is of negligible size in magnetar X-ray spectra and contributes $\ll 1\%$ of the total flux.

Energy absorbed from the X mode field in the vacuum resonance heats the local plasma. There is substantial variation in the precise depth at which the absorption will occur across the soft X-ray band (31) and the net effect is the formation of an opaque “heating layer” in the atmosphere (Figure 11). The influence of this absorption on the emergent spectrum depends on the proximity of the absorbing layer to the X mode decoupling layer. Both the density of resonant absorption and the amplitude of the X mode opacity resonance induced by vacuum corrections *decline* with photon energy. Radiation of sufficiently low frequency will have only modest interaction with the opaque layer and will retain the plasma dominated photosphere ($\tau_E^{vp} \ll 1$). This may be contrasted with radiation which decouples from within the opaque layer because of the large optical depth accumulated at ρ_{res} . For the 10^{14} G models illustrated, this transition occurs at $\sim 1.5 - 3.0$ keV. Figure (12) shows the decoupling density of these strongly magnetized models. At energies $\gtrsim 3$ keV, the X mode radiation decouples from somewhat cooler strata than would be found were VP effects neglected; no radiation decouples from the relatively tenuous vacuum dominated plasma ($\tau_E^{vp} \gg 1$) and the response properties characteristic of this regime have no influence on either the polarization or angular distribution of the spectra (see §2.2).

Thermal absorption in the opaque heating layer has an ancillary effect on the spectrum at long wavelengths which decouple below the layer, where the flux amplitude is enhanced by the re-radiated emission. The formation depth of the proton cyclotron line becomes comparable to the depth of the heating layer, which reduces the effective width of the proton cyclotron line in the 10^{14} G models. For models $\log T_{eff} \gtrsim 6.5$ the cyclotron absorption line is preserved but narrower than expected from the equivalent model without vacuum corrections (Fig. 13). For cooler T_{eff} , the formation depth of the line coincides with larger T than for neighboring frequencies, leading to an apparent emission feature. Regardless of T_{eff} , the reduced effective width of the line results from enhanced thermal emission from the opaque layer. That this transformation occurs over a range of just $2.5 T_{eff}$ suggests that this feature may be of diagnostic value in thermal spectra of some anomalous X-ray pulsars. Figure (14) summarizes the evolution in cyclotron temperature with T_{eff} .

6 DISCUSSION

Observations of thermal spectra from cooling isolated NSs provide a direct probe of their surface properties, assuming these data can be adequately interpreted with a realistic spectral model. The surface magnetic field strength can be measured through the detection of cyclotron features. Strong atomic transitions constrain the ratio M/R , while an additional measure of the gravitational potential (e.g. through line profiles) could restrict M and R individually (Paerels 1997); line broadening mechanisms and variation of surface properties pose additional difficulty for interpretation of these properties. With the exception of 1E 1207.4-5209 for which the nature of absorption features is presently uncertain, the failure to measure *any* spectral features in the *Chandra* and *XMM* observations

of thermally emitting NS is notorious. Non-detection of features in NS surface emission tends to favor light element atmosphere models; the Fe atmospheres of Rajagopal et al. (1997) for example predict strong absorption edges at soft X-ray energies which should be unambiguous in the data. The absence of cyclotron features may exclude ranges of surface field strength but, for well magnetized stars, such features can be smoothed by realistic distributions of the surface temperature and field (Zane et al. 2001). Measurement of the integrated net polarization at X-ray energies for cooling, isolated NS may provide enough information to deduce the surface magnetic field strength where spectral features remain unresolved or are destroyed by other processes (Pavlov & Zavlin 2000; Heyl et al. 2003).

We have presented a flexible, efficient and robust method for computation of light element thermal NS spectra and atmospheric structures. The radiative processes in these models are the simplest required to describe the X-ray properties of cooling light element NS atmospheres for a broad range of stellar parameters. A number of refinements to the model physics and distinguishing elements of the present work are described below.

Ionization equilibrium — In strong magnetic fields the ground state binding energy of stationary Hydrogen atoms grows asymptotically with $\sim \ln^2 B_c$ Ryd where $B_c = B/2.35 \times 10^9$ G (Louden 1959), and bound state transitions may become important to the X-ray spectrum of NS at 10^{12} G. Motional effects of the atoms within strong magnetic fields leads to the formation of decentered states, and yields substantially altered cross sections (Potekhin 1998). Pavlov et al. (1995) have shown that even a modest neutral plasma component can alter the spectrum owing to bound-free transitions from these tightly bound states. Moreover, pressure destruction is less effective in strong magnetic fields owing to the reduce phase space volume accessible to the electron distribution. An occupation probability (OP) formalism has been studied in detail for both magnetized Potekhin et al. (1999) and unmagnetized Hydrogen plasma (Potekhin 1996). This free-energy picture is parametrized by the binding energies and mean atomic sizes, and provides a natural equation of state governing the pressure destruction of weakly bound states and truncation of the partition function. Steady progress has been made in the EOS for magnetized hydrogen, and a recent report describes an effort to integrate the ionization equilibrium of Potekhin & Chabrier (2002) with the Lucy-Unsöld temperature correction scheme (Ho et al. 2002).

It is more challenging to incorporate non-LTE processes to the statistical equilibrium, by which the bound state distributions are determined through detailed balance of the collisional and radiative rate coefficients. The radiative rates can be evaluated by straightforward integration given (e.g.) the bound-free cross sections and the state of the radiation field. The collisional transition rates must also be specified, unlike LTE in which it is sufficient to consider ratios of these rates and which are given by Boltzmann factors; these rates, and preferably their derivatives, must be computed or otherwise tabulated for the spectrum of bound states and continuum. The CL technique is able to respond to neutral or incompletely ionized component better than Lucy-Unsöld upon simultaneous integration of the statistical equilibrium and radiative transfer, but may require adaptive depth points around the transition zones between successive ionization states or near line formation depths. Much simpler would be inclusion of OPAL opacities in the present code (see e.g. Werner & Deetjen (2000) or Gänsicke et al. (2002)) but these tabulations are not appropriate for strongly magnetized atmospheres. The ionized model calculations described in this paper underutilize the advantages afforded by the CL method.

High density effects — Two phenomena related to dense plasma are not accounted for in the opacity formulation of §2. Collective plasma effects are encountered where $v_e > 1$ strongly influence the optical and near UV flux of thermal models with radio pulsar type fields (Fig. 6); the effects extend to X-ray energies for the magnetar models (Fig. 12). In this regime, the collective response of the plasma should strongly attenuate propagating waves, and the assumption of radiative transport may be incorrect to long wavelength radiation. This is plain in the magnetar spectra, but is also relevant at optical wavelengths for very cool stars (e.g. RXJ 1856.35) and aging RPs like Geminga. Collective phenomena may be included by way of a structure factor in the scattering opacity as a first step toward evaluating corrections to the equilibrium thermal structure. Secondly, plasma is tightly coupled when $\Gamma \equiv (4\pi n_e/3)^{1/3} e^2/(kT) > 1$, but the Debye-Hückel approximation (48) is only a perturbative correction. A more plausible model for P_{Coul} could be implemented, although errors in the coupling occur at the very deepest model strata of the most strongly magnetized atmospheres where an improved calculation is likely to correct only the X mode intensities in the spectral tail.

Ionic cyclotron resonances — Our opacity calculation is derived from the self-consistent inclusion of ions in the plasma dielectric (2); energy dependencies which scale with magnetic field enter the opacity through the eigenvalues of the polarization tensor (20). Some authors favor a calculation of these eigenvalues in which electrons and protons are distinct plasma constituents, with effective eigenvalues (c.f. Zane et al. (2000); Ho & Lai (2001)):

$$\pi_{p,eff}^2 \simeq \frac{1}{(1 - pu_e^{1/2})^2} + \frac{(m_e/m_p)^2}{(1 + p \frac{m_e}{m_p} u_e^{1/2})^2} \quad (61)$$

As discussed in §2.1 the principal source of ion cyclotron absorption resides in resonant behavior of the polarization vector itself and, if the vectors e_p^j are computed consistently as described in §2, the discrepancy of no particular consequence for radiation $\omega > \omega_{c,p}$; the opacity to longer wavelength radiation however acquires a scaling factor $\propto u_e^{-2}$ from eqn (20), which is steeper than the $\sim u_e^{-1}$ scaling of (61). Results calculated in the approximation (61) are potentially unreliable at X-ray energies for $B \gtrsim 10^{14}$ G, and the discrepancy is compounded for admixtures of helium.

Warm plasma and other opacity effects — The opacity model of §2 is derived assuming “cold” electron plasma plus vacuum and neglects plasma dispersion which is of interest near the electron cyclotron line (Kirk & Mészáros 1980). We have also neglected Comptonization which affects the amplitude of the high energy spectral cutoff (Kaminker et al. 1983). For the NS model temperatures discussed herein, a fully relativistic treatment of the plasma response is unnecessary (Mészáros 1992). Calculation of the magnetic Gaunt factors at transitional field strengths $\ell \sim 1$ are incomplete as described in §2 and could be improved by using the calculation of Pavlov & Panov (1976).

REFERENCES

- Adler, S. L., 1971, Ann. Phys., 67, 599
- Antia, H. M., 1993, ApJS, 84, 101
- Auer, L. H., Mihalas, D., 1968, ApJ, 151, 311
- Auer, L. H., Mihalas, D., 1969, ApJ, 158, 641
- Auer, L., 1976, JQSRT, 16, 931
- Auer, L. H., Heasley, J. N., House, L. L. 1977, ApJ, 216, 531
- Brown, E. F., Bildsten, L., Rutledge, R. E., 1998, ApJ, 504, L95
- Bulik, T., Pavlov, G. G., 1996, ApJ, 469, 373

Chiu, H.-Y., Salpeter, E. E., 1964, Phys. Rev. Lett., 12, 413
 Clayton, D. D., 1983, "Principles of Stellar Evolution and Nucleosynthesis" (Univ. of Chicago)
 Gänsicke, B. T., Braje, T. M., Romani, R. W., 2002, A&A, 386, 1001
 Gnedin, Yu. N., Pavlov, G. G., 1975, Sov. Phys. JETP, 38, 903
 Heyl, J. S., Hernquist, L., 1997, J. Phys. A, 30, 6475
 Heyl, J. S., Hernquist, L., 1998, MNRAS, 298, L17
 Heyl, J. S., Shaviv, N., Lloyd, D. A., submitted to MNRAS
 Ho, W. C. G., Lai, D., 2001, MNRAS, 327, 1081
 Ho, W. C. G., Lai, D., 2002, astro-ph/0201380
 Ho, W. C. G., Lai, D., Potekhin, Y., Chabrier, G., 2002, astro-ph/0212077
 Ho, W. C. G., Lai, D., 2003, MNRAS, 338, 233
 Iglesias, C. A., Rogers, F. J., Wilson, B. G., 1987, ApJ, 322, L45
 Itoh, N., Sakamoto, T., Kusano, S., Nozawa, S., Kohyama, Y., 2000, ApJS, 128, 125
 Kaminker, A. D.; Pavlov, G. G., Shibanov, Yu. A., 1983 Ap&SS, 91, 167
 Kirk, J. G., Mészáros, P., 1980, ApJ, 241, 1153
 Krishna-Swamy, K. S., 1961, ApJ, 134, 1017
 Lloyd, D. A., Hernquist, L., Heyl, J. S., 2003, submitted to ApJ
 Loudon, R. 1959, Am. J. Phys., 27, 649
 Mészáros, P. 1992 "High-Energy Radiation from Magnetized Neutron Stars" (Univ. of Chicago)
 Mészáros, P., Ventura, J., 1979, Phys. Rev. D, 19, 3565
 Mihalas, D. 1978 "Stellar Atmospheres" (Freeman)
 Özel, F. 2001, ApJ, 563, 276
 Paerels, F., 1997, ApJ, 476, L47
 Pavlov, G. G., Panov, A. N., 1976, Sov. Phys. JETP, 44, 300
 Pavlov, G. G., Shibanov, Yu. A., 1979, Sov. Phys. JETP, 49, 741
 Pavlov, G. G., Shibanov, Yu. A., Zavlin, V. E., 1992, MNRAS, 253, 193
 Pavlov, G. G., Shibanov, Yu. A., Ventura, J., Zavlin, V. E., 1994, Astron. Astrophys. 289, 837
 Pavlov, G. G., Shibanov, Yu. A., Zavlin, V. E., Meyer, R. D., 1995, "The Lives of Neutron Stars", 71, ed. M.A. Alpar et al. (Kluwer)
 Pavlov, G. G., Zavlin, V. E., Trümper, J., Neuhäuser, R., 1996, ApJ, 472, L33
 Pavlov, G. G., Zavlin, V. E., 2000, ApJ, 529, 1011
 Potekhin, A. Y., 1996, Phys. Plasmas, 3, 4156
 Potekhin, A. Y., 1998, J. Phys. B.: At. Mol. Opt. Phys., 31, 49
 Potekhin, A. Y., Chabrier, G., Shibanov, Y. A., 1999, Phys. Rev. E, 60, 2193
 Potekhin, A. Y., Chabrier, G., 2002, astro-ph/0212062
 Rajagopal, R., Romani, R. W. 1996, ApJ, 461, 327
 Rajagopal, R., Romani, R. W., Miller M. C. 1997, ApJ, 479, 347
 Romani, R., 1987, ApJ, 313, 718
 Shibanov, Yu. A., Zavlin, V. E., Pavlov G. G., Ventura, J., 1992, Astron. Astrophys., 266, 313
 Soffel, M., Ventura, J., Herold, H., Ruder, H., Nagel, W., 1983, A&A, 126, 251
 Sutherland, R. S., 1998, MNRAS, 300, 321
 Tsuruta, S., 1964, Ph.D. thesis, Columbia Univ.
 Ventura, J., 1979, Phys. Rev. D, 19, 1684
 Werner, K., Deetjen, J., 2000, in "Pulsar Astronomy - 2000 and Beyond", eds. M. Kramer, N. Wex, and N. Wielebinski, ASP Conference Series, Vol. 202, 623
 Zane, S., Turolla, R., Treves, A., 2000, ApJ, 537, 387
 Zane, S., Turolla, R., Stella, L., Treves, A., 2001, ApJ, 560, 384
 Zavlin, V. E., Pavlov, G. G., Shibanov, Yu. A., Ventura, J., 1995, Astron. Astrophys. 297, 441

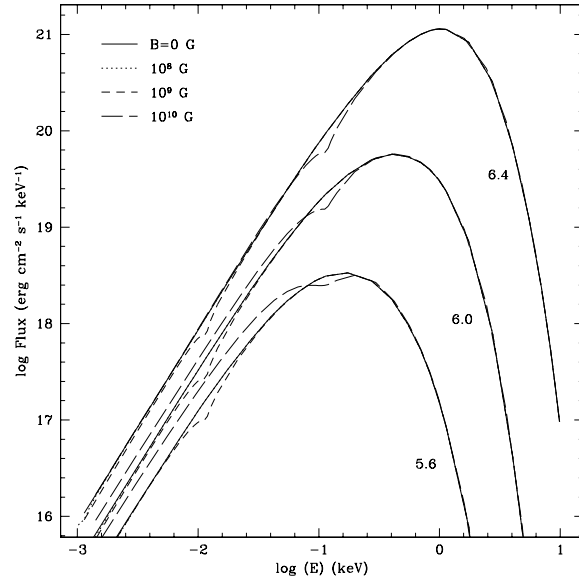


Figure 1. Total emergent flux profiles for unmagnetized Hydrogen plasma atmosphere (solid curves), and weakly magnetized plasma $\log B = 8.0(1.0)10.0$ G, at three effective temperatures $\log T_{\text{eff}} = 5.6(0.4)6.4$. For $\log B = 10.0$ the cyclotron absorption encroaches on the soft X-ray spectrum, and at lower T_{eff} becomes comparable to the peak emission, yielding enhanced optical and near UV amplitudes. With the exception of the coolest $\log B = 10.0$ atmospheres, the model spectra satisfy a single displacement rule $E_{\gamma}^{\text{max}} \simeq 4.7kT_{\text{eff}}$.

Zavlin, V. E., Pavlov, G. G., Shibanov, Yu. A., Rogers, F. J., Iglesias, C. A., 1996, in "Roentgenstrahlung From the Universe", ed. H.U. Zimmermann, J.E. Trümper, H. Yorke, MPE Report 263
 Zavlin, V. E., Pavlov, G. G., Shibanov, Yu. A., 1996, Astron. Astrophys., 315, 141
 Zavlin, V. E., Pavlov, G. G., astro-ph/0206025

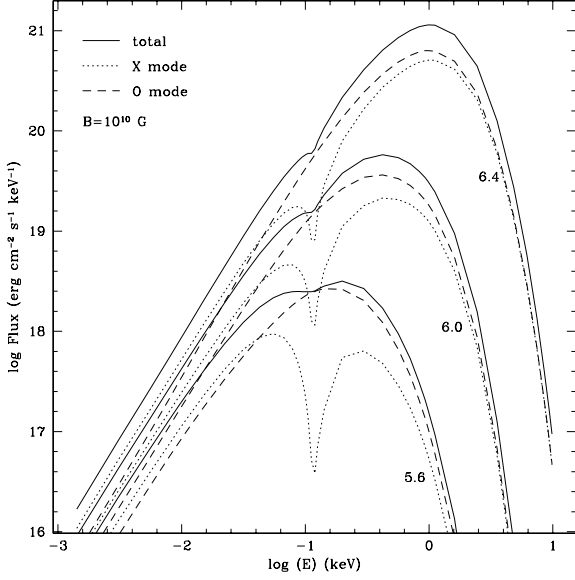


Figure 2. Spectral envelopes for $\log B = 10.0$ at three flux temperatures, $\log T_{\text{eff}} = 5.6(0.4)6.4$; resonant absorption significantly affects the spectrum where the electron cyclotron feature is nearly coincident with peak emission energy. Only X-mode radiation is sensitive to electron cyclotron absorption, and energy thus absorbed is reemitted at longer wavelengths.

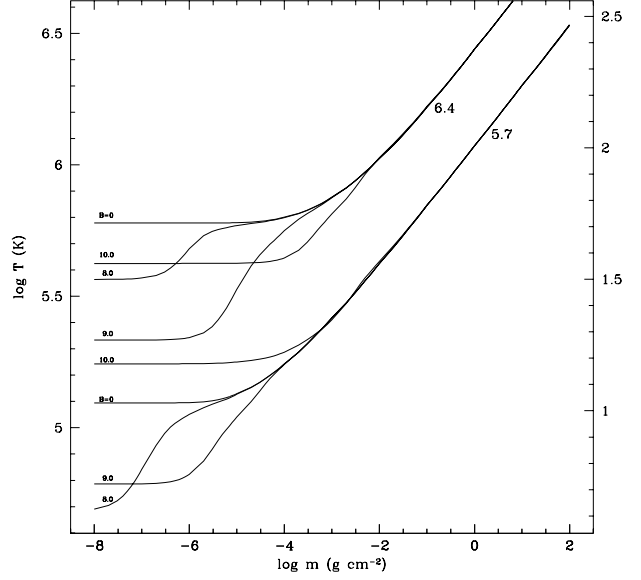


Figure 4. Temperature profiles for several converged, weakly magnetized models, illustrating the variation in asymptotic surface temperature which results from energy redistribution from cyclotron absorption in a radiative equilibrium atmosphere. Curves are labelled by $B = 0$ (unmagnetized) or $\log B$. At finite B , departures from the unmagnetized thermal structure occur at deeper strata for increasing field strength.

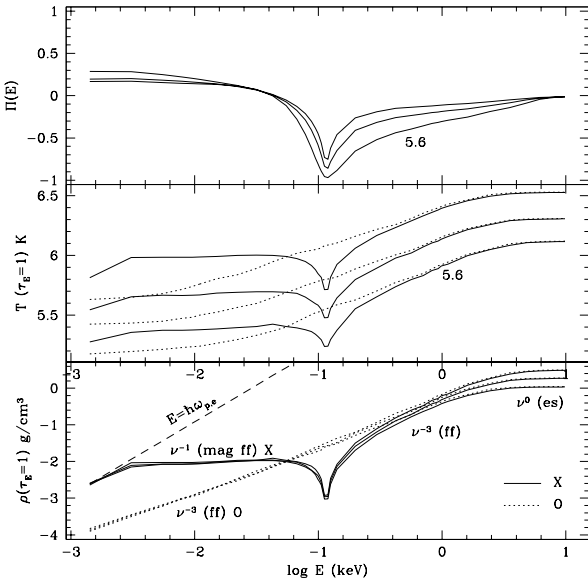


Figure 3. Polarization fraction (upper), photospheric temperature (middle) and decoupling density (lower panel) for the model spectra of Fig 2. Resonant absorption plays a more significant role at cooler temperatures, where the peak thermal energy approximately coincides with the cyclotron line. Thomson scattering of high energy photons is energy independent; lower energy photons which are predominantly absorbed decouple from similar densities regardless of T_{eff} .

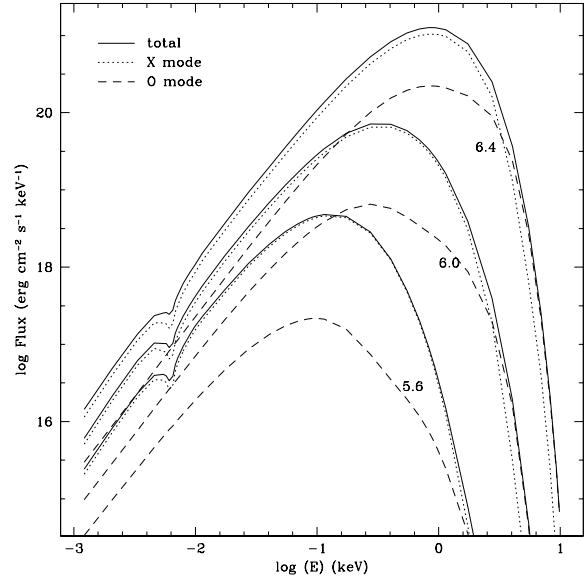


Figure 5. Model spectra for $\log B = 12.0$ and $\log T_{\text{eff}} = 5.6(0.4)6.4$ including the partial polarized flux contributions. The broad electron cyclotron line is centered off diagram at $E \sim 11.6$ keV, but its influence is seen in the relative amplitude of emission in the two modes.

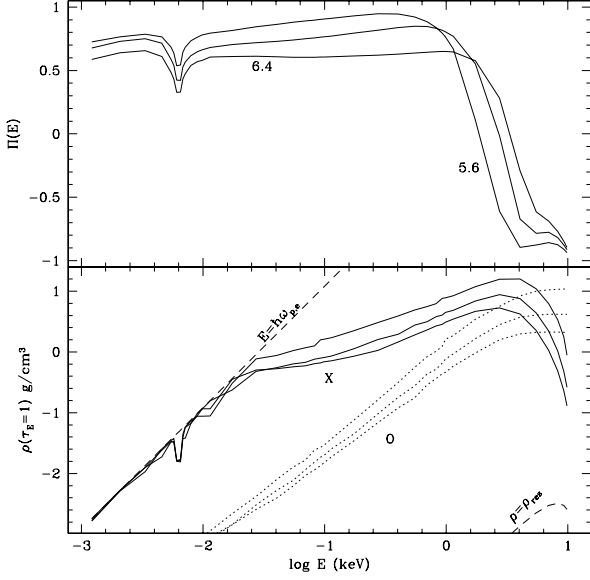


Figure 6. Polarization and decoupling density for the model spectra of Fig (5). Radiation near the electron feature have large negative $\Pi(E)$ owing to the relatively large O mode amplitude (upper panel). The proton line demonstrates modest variation in net polarization. The ν^{-1} dependence of the X mode opacity is more apparent than for the 10^{10} G models (lower panel). Models with higher T_{eff} decouple at greater ρ . Measurement of $\Pi(E)$ in two bands may be sufficient to diagnose T_{eff} for surface fields $B \simeq 10^{11} - 10^{13}$ G.

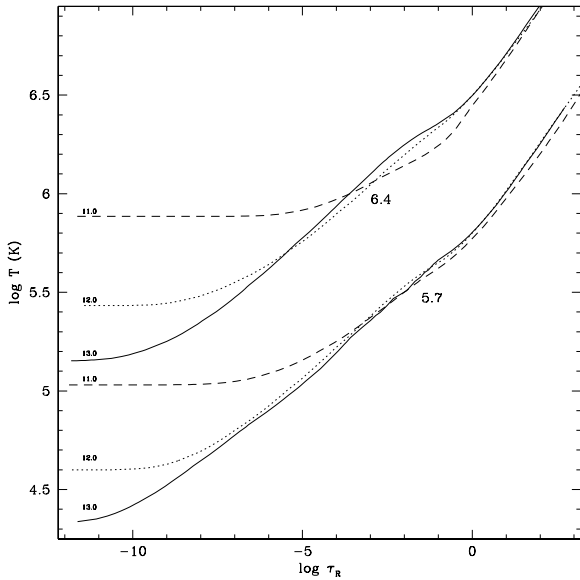


Figure 7. Equilibrium temperature profiles on the mean Rosseland depth scale for $\log T_{\text{eff}} = 5.7, 6.4$ with intermediate magnetic fields $\log B = 11.0(1.0)13.0$. As B increases, a greater fraction of the total flux is emitted in the (transparent) X mode from deep, hot strata. The asymptotic surface temperature declines with increasing field strength owing to the depleted intensity in the more opaque O mode.

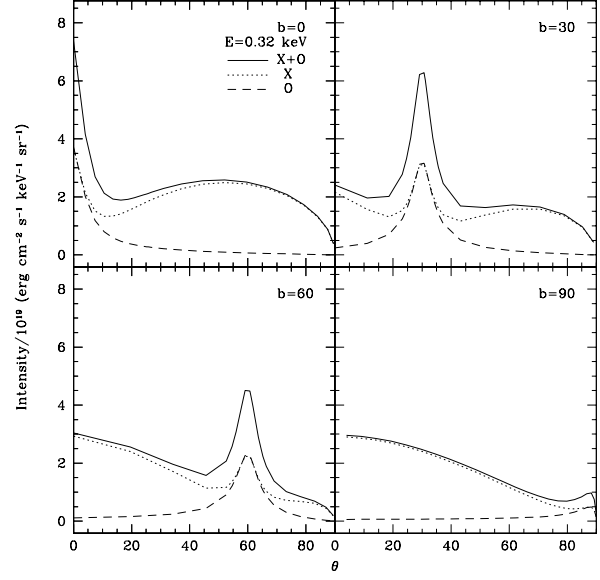


Figure 8. Angular intensity profiles near the spectral peak for $\log T_{\text{eff}} = 6.0$, $\log B = 12.0$, and four choices of magnetic field orientation. For each curve the vectors \vec{B} , \vec{k} , \vec{n} are coplanar ($\phi = 0$). Intensity along the field vector declines with increasing inclination by decoupling from lower temperatures in higher strata. The pencil beam has approximately equal contributions from both modes while the fan emission is highly polarized.

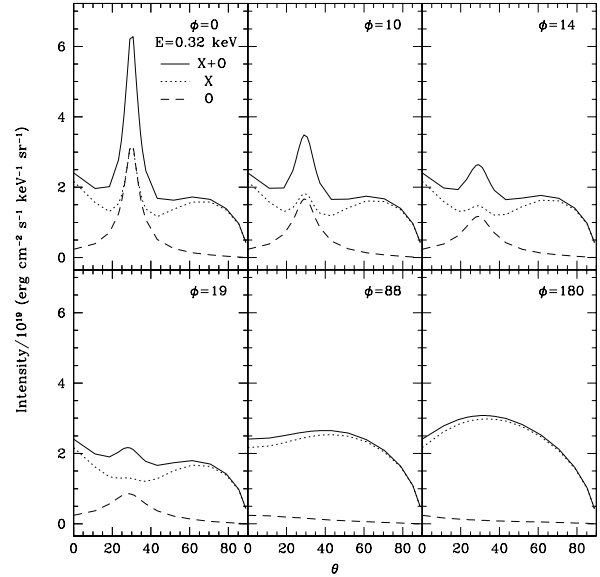


Figure 9. Angular intensity profiles for $B = 10^{12}$, $T_{\text{eff}} = 10^6$ and $b = 30^\circ$ at a photon energy near the spectral peak for six choices of model azimuths. The pencil amplitude declines and acquires finite polarization for $\phi > 0$ and vanishes for $\phi \gtrsim \theta_p$ and the fan component dominates for large ϕ .

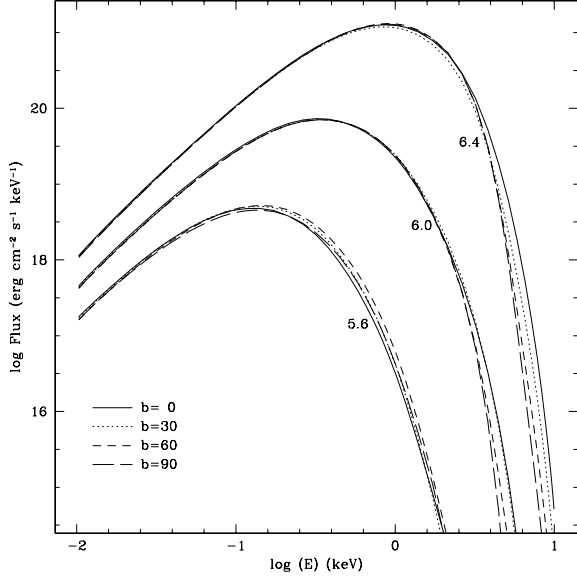


Figure 10. Total flux profiles for $\log B = 12.0$, $\log T_{\text{eff}} = 5.6(0.4)6.4$ and inclinations $b = 0, 30, 60, 90$. Spectra for $T_{\text{eff}} \gtrsim 6.0$ are softer at high energies for larger field inclinations. The converged $T(m)$ for these models do not reveal large variation with b for a given T_{eff} .

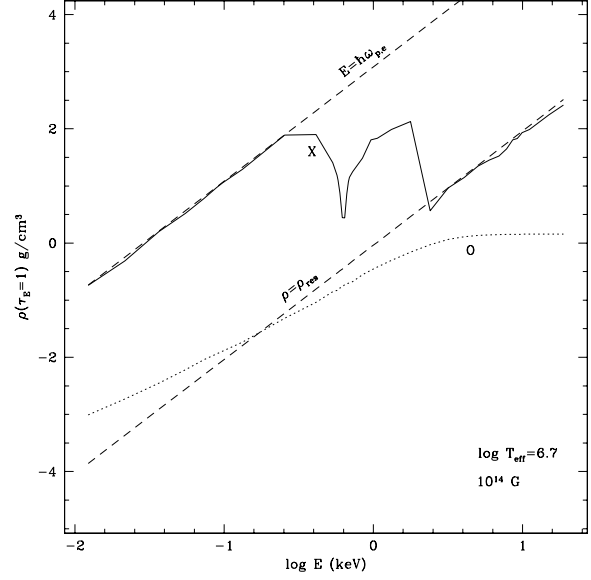


Figure 12. The decoupling density for $B = 10^{14}$ G at $\log T_{\text{eff}} = 6.7$, illustrating the transition to photosphere formation within the vacuum resonance layer above 1.5 keV. The X-mode flux below 0.25 keV is dominated by collective plasma effects.

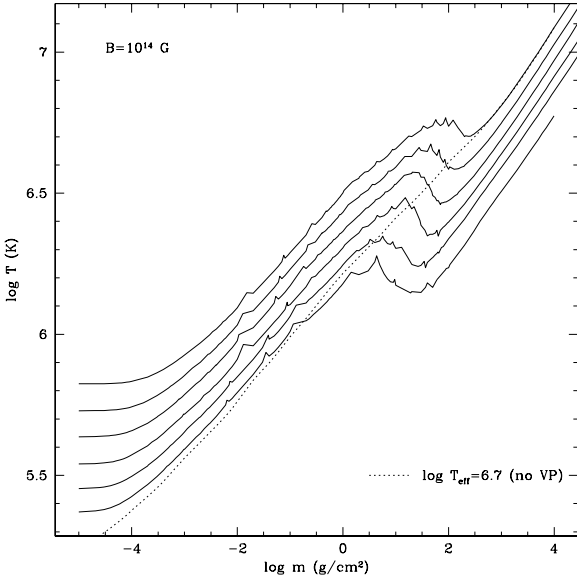


Figure 11. Thermal structure of the magnetar models $B = 10^{14}$ G for a range of effective temperatures $\log T_{\text{eff}} = 6.2(0.1)6.7$. The effect of the vacuum resonance on the transparent X mode is clearly seen in the form of the heating layer. Small “jumps” in the temperature profiles arise from abrupt variation in opacity at the adaptive depth points, particularly for energies $E \gtrsim 1$ keV. The dashed profile is that of the converged model for pure plasma at $\log T_{\text{eff}} = 6.7$ and $B = 10^{14}$ G.

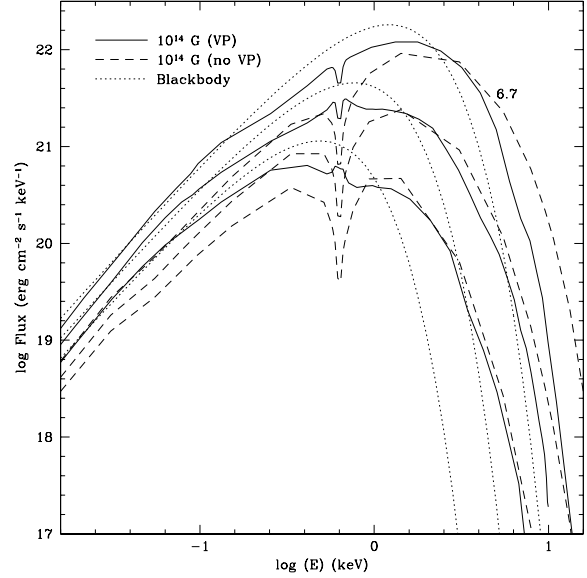


Figure 13. Total flux profiles for $\log T_{\text{eff}} = 6.3(0.2)6.7$ at 10^{14} G, comparing the vacuum polarized models (solid curves) to their ordinary plasma equivalents (long dash). Reemission of thermal radiation absorbed in the opaque layer (vacuum resonance) effectively “fills in” the proton cyclotron line in hot models, and inverts the line profile in relatively cool models.

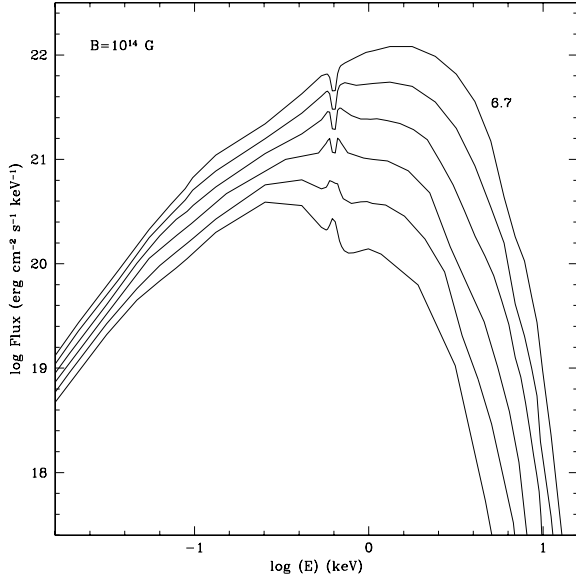


Figure 14. The flux profiles for the magnetar models $B = 10^{14}$ G for the effective temperatures $\log T_{\text{eff}} = 6.2(0.1)6.7$. The width of the proton cyclotron line is reduced by the incidental effects of vacuum polarization on the atmospheric structure (Fig 11). This phenomenon is ultimately responsible for line “inversion” in cooler models.